




Article

# Annealing-Induced Changes in the Microstructure and Mechanical Response of a Cu Nanofoam Processed by Dealloying

Péter Jenei <sup>1</sup>, Csilla Kádár <sup>1,2,3</sup>, Gigap Han <sup>4</sup>, Pham Tran Hung <sup>1</sup>, Heeman Choe <sup>4</sup> and Jenő Gubicza <sup>1,\*</sup>

<sup>1</sup> Department of Materials Physics, Eötvös Loránd University, P.O. Box 32, H-1518 Budapest, Hungary; jenei@metal.elte.hu (P.J.); kadar@eik.bme.hu (C.K.); hungpthung95@gmail.com (P.T.H.)

<sup>2</sup> Department of Materials Science and Engineering, Budapest University of Technology and Economics, Műgyetem rakpart 3., H-1111 Budapest, Hungary

<sup>3</sup> MTA–BME Lendület Composite Metal Foams Research Group, Műgyetem rakpart 3., H-1111 Budapest, Hungary

<sup>4</sup> School of Materials Science and Engineering, Kookmin University, 77 Jeongneung-ro, Seongbuk-gu, Seoul 02707, Korea; hgg4602@gmail.com (G.H.); choeheeman@gmail.com (H.C.)

\* Correspondence: jeno.gubicza@ttk.elte.hu; Tel.: +36-1-3722876

Received: 12 July 2020; Accepted: 19 August 2020; Published: 21 August 2020



**Abstract:** Cu nanoporous foams are promising candidates for use as an anode material for advanced lithium ion batteries. In this study, Cu nanofoam was processed from pack-cemented bulk material via dealloying. In the as-processed Cu nanofoam, the average ligament size was ~105 nm. The hardness in this initial state was ~2 MPa, and numerous cracks were observed in the indentation pattern obtained after hardness testing, thus indicating the low mechanical strength of the material. Annealing for 6 h under an Ar atmosphere at 400 °C was shown to result in crystalline coarsening and a reduction in the probability of twin faulting in the ligaments. Simultaneously, the junctions of the ligaments became stronger and hence more difficult to crack. This study demonstrates that moderate heat treatment under Ar can improve the resistance against crack propagation in Cu nanofoam without a large change in the ligament size and the surface oxide content, which can thus influence the electrochemical performance of the material in battery applications.

**Keywords:** Cu nanofoam; dealloying; hardness; cracking; annealing

## 1. Introduction

Novel rechargeable batteries are a prerequisite for the sustainable development of the modern human lifestyle. The most frequently used battery type is the lithium ion battery (LIB) [1–3]. Although the conventionally used graphite anode displays good charging/discharging stability, its theoretically low capacity limits the potentially promising modern applications of LIBs [4]. Therefore, new anode and cathode materials with higher capacities are targeted for further development in the industry. In this regard, carefully designed open-pore metallic foams are promising candidates for use as an advanced LIB anode [5–8]. The internal surface of such foams can be covered by a high-capacity active layer which can take up and store Li ions [7]. For example, the surface layer may take the form of an artificially generated Cu oxide film (theoretical capacity 674 mAh/g [9]) or tin film (theoretical capacity 993 mAh/g [10]) on the ligaments of the Cu foam. The high porosity of the foam yields a large specific surface area, thereby increasing the charge storage capacity and perhaps the power of the anode material. In other words, the internal space in the foam can accommodate the volume expansion that occurs in the high-capacity active material during lithiation, thus reducing the internal

stresses developed during the charging/discharging cycle and enhancing the operation lifetime of the anode. Metallic foams for LIB anodes have been manufactured using various techniques such as sintering, freeze-casting, or dealloying [7,11–13]. With the use of the dealloying method, nanoporous or even hierarchically structured metal foams can be manufactured from bulk materials via the pack cementation process [7]. We found that one major weakness of the dealloyed nanoporous metal foams is their tendency to brittleness. Hence, in the present paper, the mechanical properties of a dealloyed nanoporous Cu were shown to be improved by annealing at a moderate temperature. The annealing-induced change in the Cu nanofoam microstructure was analyzed and correlated with its improved mechanical performance.

## 2. Materials and Methods

### 2.1. Synthesis of Nanoporous Cu

A Cu nanofoam was synthesized from a pack-cemented bulk precursor material via dealloying. In the first step, a blend of Al, Al<sub>2</sub>O<sub>3</sub>, and NH<sub>4</sub>Cl powders was mixed and stacked on a Cu disk with a diameter of 11 mm (a common size for a 2032-type coin cell) and a thickness of 0.25 mm in a stainless-steel container. In the pack-cementation step, the specimen was heat-treated at 800 °C for 6 h. During this heat treatment, the Al particles were melted, and Al atoms diffused into the Cu, thus forming the Al<sub>2</sub>Cu phase [7]. The Al<sub>2</sub>O<sub>3</sub> filler in the powder blend was used to slow the process and control the coating uniformity by decreasing the effective surface of the disk [7]. After the pack-cementation process, the material was annealed at 700 °C for 9 h, and then at 500 °C for a further 6 h, in order to homogenize the Al distribution in the Al<sub>2</sub>Cu phase. The pack-cemented bulk sample was mechanically grinded with abrasive grinding papers (1000, 2500, and 4000 grit sizes) and polished with 1 μm Al<sub>2</sub>O<sub>3</sub> suspension. After the surface treatment, the pack-cemented bulk sample was cut into two halves so that one half could be subjected to further annealing after dealloying. In the dealloying process, the two sample parts were chemically etched in aqueous HCl at 45 °C for 24 h in order to remove the Al atoms from the material. The pH of the HCl solution was set at 0.25. After dealloying, the etched samples were washed in ethanol and dried at 0.8 bar for 5 min. Subsequently, one sample was annealed at 400 °C for 6 h under an Ar atmosphere using a Perkin Elmer (DSC2) differential scanning calorimeter. This temperature corresponds to a homologous temperature of 0.5. The dealloyed foam and its annealed counterpart are denoted hereafter as the initial and heat-treated specimens, respectively. A schematic of the processing steps of the samples is shown in Figure 1.

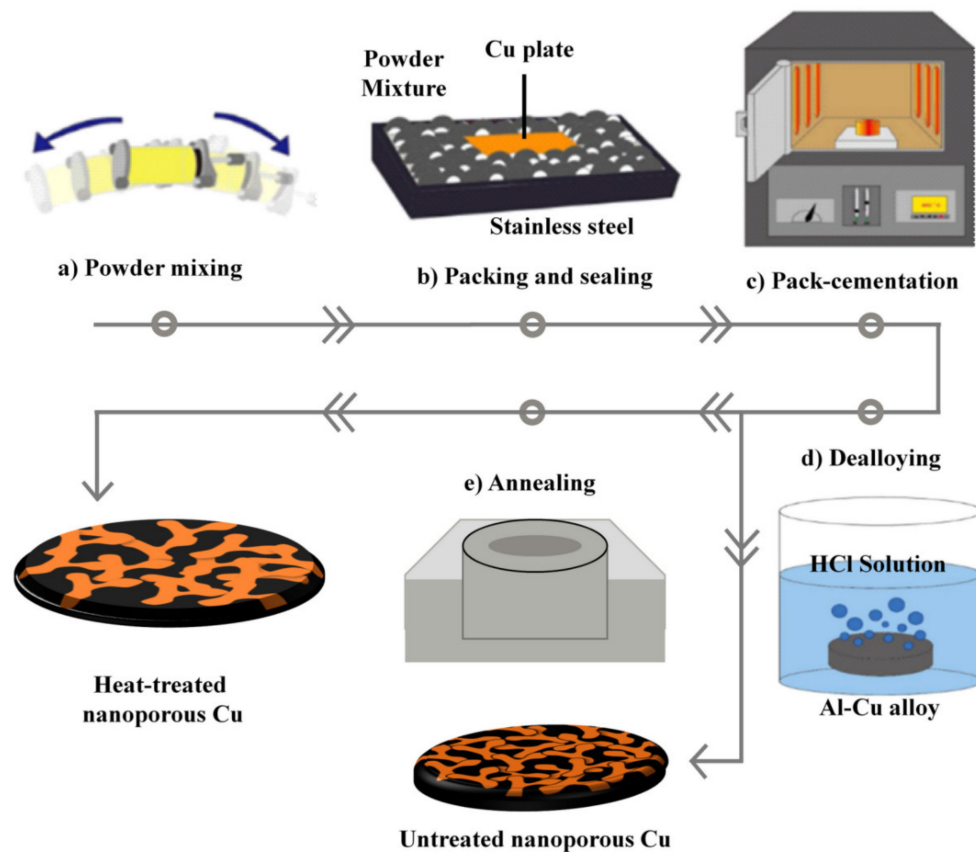


**Figure 1.** Schematic diagram of the novel processing method proposed in this study to create nanoporous Cu foam using a pack cementation Al coating process on Cu foil.

## 2.2. Characterization of the Microstructure

The phase composition of both the initial and heat-treated specimens was investigated by X-ray diffraction (XRD) using a Smartlab X-ray powder diffractometer (Rigaku, Tokyo, Japan) with  $\text{CuK}\alpha_1$  radiation (wavelength: 0.15406 nm). The size and morphology of the ligaments of the foams were studied using scanning electron microscopy (SEM) with an FEI Quanta 3D electron microscope (Thermo Fisher Scientific, Waltham, MA, USA). The average ligament size was obtained using a standard metallographic method in which straight lines were placed randomly on the images, and the average length of the segments of the straight lines lying inside the ligaments was determined. Additionally, the degree of continuity of the nanoporous Cu ligament was also assessed metallographically using the contiguity parameter ( $C_5$ ) defined in Section 3. The chemical composition of the foam ligaments was investigated by energy dispersive X-ray spectroscopy (EDS) in SEM, using an electron energy of 20 keV.

The diffraction domain size and the lattice defect structure in the Cu ligaments were studied by X-ray line profile analysis (XLPA). The X-ray line profiles were measured with a RA MultiMax-9 high-resolution rotating anode diffractometer (Rigaku, Tokyo, Japan) using  $\text{CuK}\alpha_1$  radiation. The XRD patterns were evaluated using the convolutional multiple whole profile (CMWP) fitting method [14,15]. In this procedure, the diffraction pattern is fitted by the sum of a background spline, the convolution of the instrumental pattern, and the calculated line profiles related to the diffraction domain size, dislocations, and twin faults. Due to the very broad diffraction peaks, instrumental correction was not necessary. This evaluation method gives the area-weighted mean diffraction domain size, the dislocation density, and the twin fault probability, where the twin fault probability in face-centered cubic (fcc) crystals is defined as the fraction of twin faults among the {111} lattice planes.

### 2.3. Hardness Testing

The change in the mechanical response of the foam due to annealing was monitored by hardness testing using a Zwick Roell ZH $\mu$  indentation machine (Kennesaw, GA, USA) with a Vickers indenter under an applied load of 10 g and a dwell time of 10 s. The average microhardness value of each sample before and after annealing was determined on the basis of 10 measurements. The foam surface under the indenter was studied with a Zeiss Axio Imager.M2m optical microscope (Oberkochen, Germany).

### 3. Results and Discussion

The XRD pattern of the initial foam (Figure 2a) indicates that the main phase was Cu, but there was also some Cu<sub>2</sub>O phase present. In addition, traces of the Cu<sub>3</sub>O<sub>4</sub> phase were detected in the diffractogram. Note that the intensity is plotted on a logarithmic scale in order to enhance the visibility of the weak peaks due to the minor oxide phases. As shown in Figure 2b, the phase composition was not very affected by the heat treatment. The composition of the chemical elements obtained from EDS are listed in Table 1, where Cu is confirmed to be the main constituent with a composition of ~90 at.%. The ~3% Al is most probably dissolved in the Cu matrix, while the oxygen content (about 6 at.%) is related to the Cu<sub>2</sub>O phase. A very small amount of Cl (~0.8 at.%) is also detected and may be derived from the NH<sub>4</sub>Cl powder used in the pack cementation procedure. The results in Table 1 also indicate no significant change in the chemical composition due to annealing.

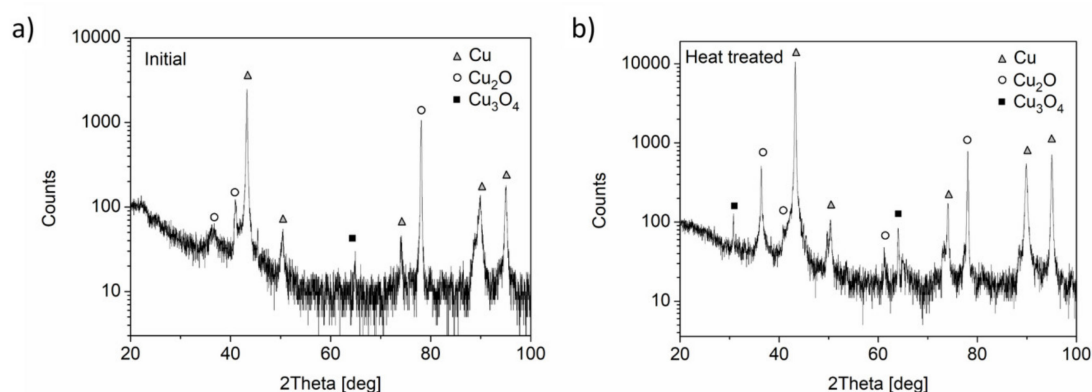


**Figure 2.** X-ray diffraction (XRD) patterns of (a) the initial as-processed Cu nanofoam and (b) the same sample annealed at 400 °C for 6 h.

**Table 1.** Chemical composition of the Cu nanofoam in the initial state and after heat treatment.

Element	Initial	Heat Treated
O (at.%)	5.6 ± 1.5	6.9 ± 0.8
Al (at.%)	3.2 ± 0.6	2.8 ± 0.1
Cl (at.%)	0.82 ± 0.14	0.63 ± 0.5
Cu (at.%)	90.3 ± 2.4	89.7 ± 0.7

The SEM image in Figure 3a reveals the microstructure of the initial Cu nanofoam, consisting of ligaments with an average size of 105 ± 6 nm (Table 2). The ligament size distribution is also indicated by the bar chart in Figure 4, which was constructed from a total of 78 measurement values. By contrast, the SEM image of the heat-treated Cu nanofoam in Figure 3b indicates the resultant coarsening of the ligaments. This is also reflected by an increase in the ligament size to 125 ± 6 nm after annealing (see also the ligament size distribution in Figure 4). Despite the relatively high heat-treatment time and temperature, the growth of the ligament size is somewhat limited. One possible explanation might be due to the considerably more coarsened average ligament size from dealloying in HCl than other solutions such as NaOH under similar conditions, which is associated with the role of surface diffusivity during dealloying; therefore, the growth rate of the relatively larger ligament in our case

could thus be lower during heat treatment [16]. Another possible explanation might be the suppressing effect of Cu oxide covering the Cu ligaments on the ligament growth, since Cu diffusion under the Cu oxide film is slower than the surface diffusion of Cu. The driving force for ligament coarsening is the decrease in the internal surface area of the nanof foam and the mechanism of coarsening is atomic diffusion. Since this process is similar to that of pressureless sintering [17], the ligament growth is expected to be accompanied by strengthening and hardening of the connecting necks via surface diffusion mass transport. Out of several important factors to be considered for the change of the global mechanical behavior of nanoporous Cu due to heat treatment, the degree of ligament contiguity (i.e., degree of ligament continuity) was investigated in this study. The value of ligament continuity was thus estimated and compared between the initial, untreated, and heat-treated nanoporous Cu by measuring the contiguity,  $C_s$ , following Fan's approach in [18] as follows:

$$C_s \approx \frac{2N^{LL}}{2N^{LL} + N^{LP}} \quad (1)$$

where  $N^{SS}$  and  $N^{SP}$  are the number of ligament/ligament and ligament/pore interface intercepts in Equation (1), respectively, within straight lines drawn randomly on the examined surfaces shown in Figure 3a,b. About 15 lines were used for each image. Each line has a length of  $\sim 1 \mu\text{m}$ . While the ligament structure in the nanoporous Cu before heat treatment is already quite continuous ( $C_s \sim 0.46 \pm 0.02$ , Figure 3a), the ligament connectivity in the nanoporous Cu after heat treatment increased further to a noticeable extent ( $C_s \sim 0.56 \pm 0.03$ , Figure 3b). Note that the contiguity value range estimated in this study ( $C_s \sim 0.46\text{--}0.56$ ) is considerably higher than that observed in nanoporous Cu processed via a powder metallurgy method ( $C_s \sim 0.3\text{--}0.4$ ) [19], suggesting that the pack-cementation method employed in this study is more advantageous in terms of the ligament continuity than the powder metallurgy method [18]. As the global mechanical behavior of nanoporous Cu with heat treatment is affected by numerous microstructural factors such as porosity/volume change, crack healing, and ligament density (in relation to pinch-off phenomenon) [20–24], a direct influence of the ligament contiguity on the mechanical properties may not be precisely determined in this case; however, the contiguity of ligament in porous metals or metal foams can be linked to their mechanical properties in other cases, as evidenced in previous literature [21,25,26].

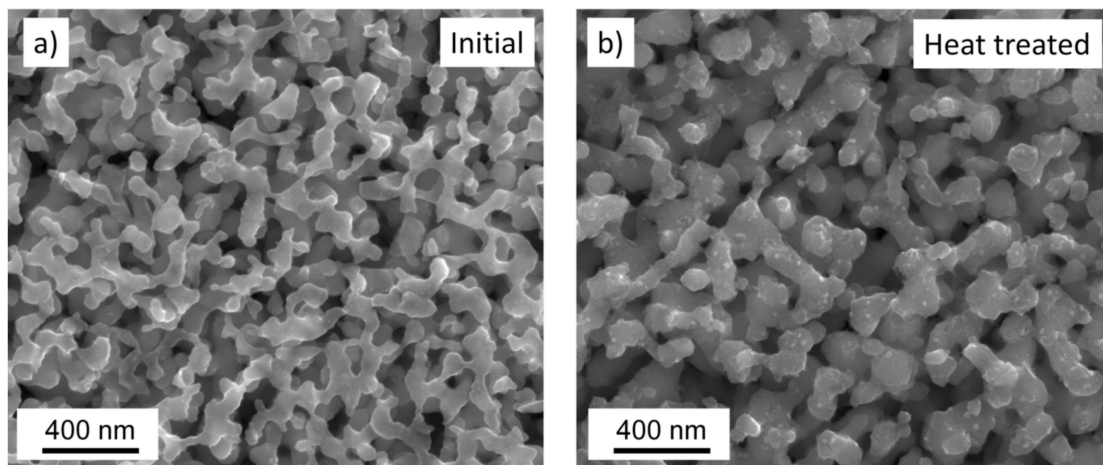


**Figure 3.** SEM images of (a) the initial as-processed foam and (b) the sample annealed at 400 °C for 6 h.

**Table 2.** Mean ligament size determined by SEM, along with average diffraction domain size, dislocation density, and twin fault probability obtained by X-ray line profile analysis (XLPA) for initial foam and heat-treated sample.

Sample	Ligament Size (nm)	Diffraction Domain Size (nm)	Dislocation Density ( $10^{14} \text{ m}^{-2}$ )	Twin Fault Probability (%)
Initial	$105 \pm 6$	$18 \pm 4$	$4 \pm 1$	$2.1 \pm 0.2$
Heat-treated	$125 \pm 6$	$142 \pm 17$	$6 \pm 1$	$1.0 \pm 0.1$

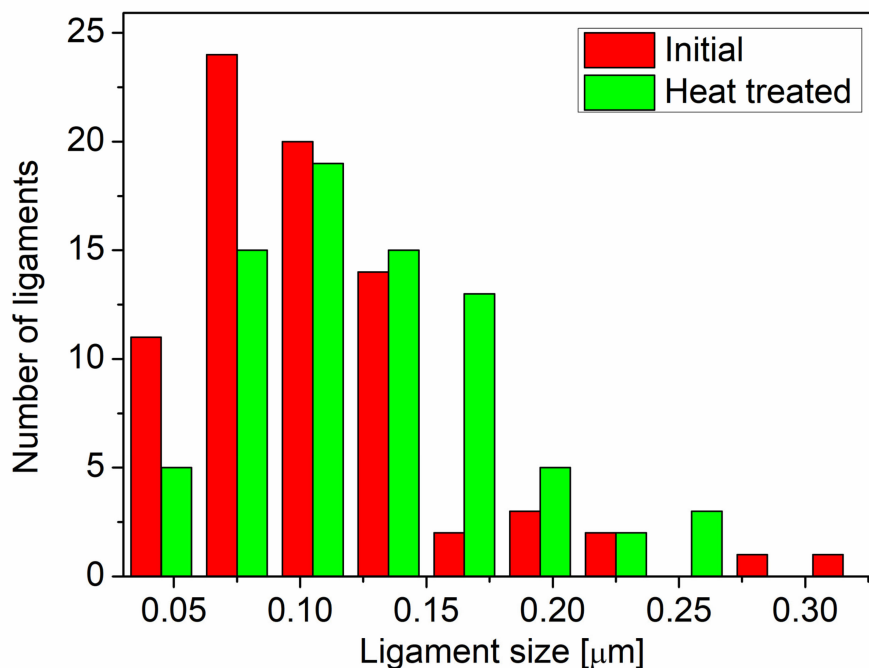


**Figure 4.** Ligament size distribution in the initial (red) and the heat treated (green) Cu foams.

Nevertheless, the hardness of the heat-treated foam ( $2.1 \pm 0.2$  MPa) was found to be essentially the same as that of the initial sample ( $1.8 \pm 0.2$  MPa). This result might be understood if the ligament interiors were softened due to the annealing of the microstructure. Therefore, the microstructure of the Cu ligaments was investigated by XLPA before and after the heat treatment. The CMWP fitting for the diffraction pattern of the initial foam is presented in Figure 5a, and the obtained microstructural parameters are listed in Table 2. Here, the diffraction domain size was seen to be 18 nm, which is much lower than the average ligament size determined by SEM. This indicates that the ligaments are fragmented into domains with various crystallographic orientations. The dislocation density and the twin fault probability were found to be  $(4 \pm 1) \times 10^{14} \text{ m}^{-2}$  and  $2.1 \pm 0.2\%$ , respectively. By contrast, the Williamson-Hall plot of the foam after the heat treatment in Figure 5b reveals a narrowing of the diffraction peaks. This is primarily due to an increase in the diffraction domain size and a decrease in the twin fault probability, as demonstrated by the CMWP fitting analysis. The results are listed in Table 2. While the dislocation density remains unchanged within experimental error, the diffraction domain size becomes comparable with the ligament size, thus indicating that the misorientations inside the ligaments disappear during annealing. In addition, the probability of twin faulting, which would obstruct dislocation glide in the ligaments, was seen to decrease from  $2.1 \pm 0.2\%$  to  $1.0 \pm 0.1\%$  due to annealing. It is noted that the decrease in the probability of as-grown twin faults during heat treatment of nanocrystalline fcc metals has already been observed in the literature. For instance, in the case of electrodeposited Ni and Ni-Mo nanocrystalline films with the grain size of about 30 nm heating up to 600–700 K at a rate of 40 K/min resulted in a decrease of the twin fault probability to about half of the initial value or less [27,28]. Both the ligament coarsening and the decrease in the probability of

twin faulting can lead to softening of the ligaments, which can, in turn, compensate for the hardening of the ligaments due to sintering. Thus, the hardness of the foam remained practically unchanged during annealing at 400 °C for 6 h.

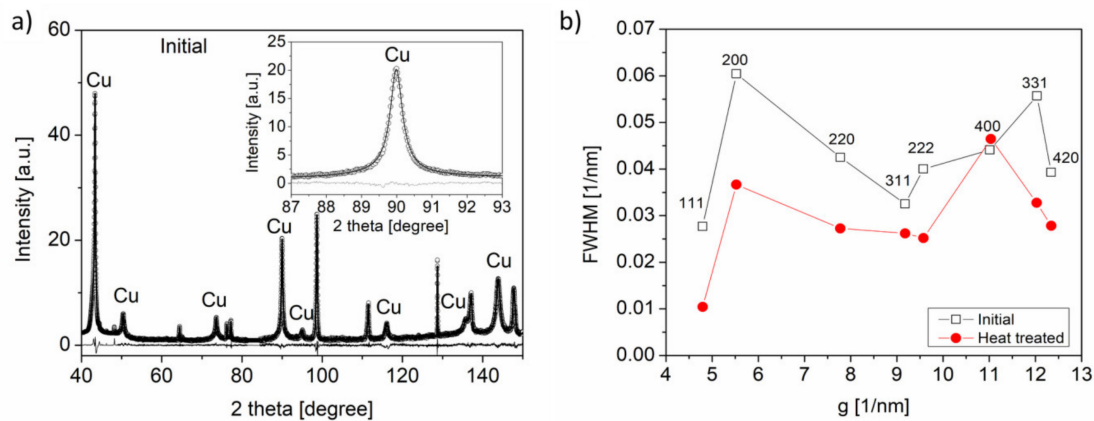


**Figure 5.** (a) Convolutional multiple whole profile (CMWP) fitting on the XRD pattern of the initial foam. The measured and the calculated diffractograms are represented by open circles and solid line, respectively. At the bottom of the figure, the difference between the measured and the calculated patterns is also shown. For the visualization of the fit quality, a magnified part of the diffractogram is shown in the inset. (b) Williamson-Hall plots for the initial and the heat-treated samples.

It should be noted that the atomic positions close to the free surface usually differ from the crystalline order valid in the particle interior. This surface relaxation yields a variation of the lattice constant along the particle diameter, thus resulting in the increase of the XRD peak width similar to the strain broadening [15]. Indeed, this phenomenon may cause an overestimation of the dislocation density. At the same time, former studies have proved that this effect becomes significant only when the fraction of surface atoms is high, namely when the particle size is smaller than about 5 nm, since only the uppermost surface layer with the thickness of about 1 nm is influenced by the surface relaxation [29,30]. For instance, in the case of a ceria powder with the mean particle size of about 4 nm, the implication of surface relaxation effect in the evaluation of the line profiles resulted in a decrease of the dislocation density by about 25% [30]. As for the present foams the average ligament size is higher than 100 nm, surface relaxation does not influence significantly the dislocation density determined by XLPA.

It is worth noting that the measured dislocation density did not change during annealing even if the temperature was high (the homologous temperature was 0.5). At the same time, the diffraction domain size increased significantly during the heat treatment. This interesting observation can be understood if we assume that the majority of dislocations are geometrically necessary dislocations (GNDs) in order to accommodate the lattice misorientations between the ligaments. Then, these dislocations are most probably located in the necks. GNDs can accommodate misorientations developed in materials processed either with or without plastic deformation. Indeed, it has been shown that GNDs with a density of  $10^{14} \text{ m}^{-2}$  can develop in spark-plasma sintered aluminum with a grain size of about 1 micron [31]. This dislocation density is of the same order of magnitude as the values determined for our foams. However, we can not provide any evidence for the existence of GNDs between the ligaments, since XLPA can not make a difference between GNDs and the statistically stored dislocations. In addition to GNDs, strains without dislocations can also develop in the necks between the ligaments. The reason for this effect is that the surface energy decreases if the contact area between the ligaments increases. At room temperature, the contact area can be increased by elastic deformation of the ligaments at the necks, resulting in elastic strains. The equilibrium configuration of a neck is reached when an infinitesimal increment of the welded contact area causes the same reduction of the surface energy as the increase in the elastic strain energy. This elastic strain causes similar XRD

peak broadening as dislocations; therefore, the dislocation density obtained by XLPD can be regarded as an effective dislocation density, including the neck strain effect. Thus, correlation between the evolutions of the domain size inside the ligaments and the strain in the necks during annealing cannot be expected.

Since both the real dislocations and the neck strains can cause similar XRD peak broadening, it is reasonable to convert the experimentally obtained dislocation density into an average root mean square strain using the following formula [15]:

$$\langle \varepsilon^2 \rangle^{1/2} = \left( \frac{\rho \bar{C} b^2}{4\pi} \ln \left( \frac{R_e}{L} \right) \right)^{1/2} \quad (2)$$

where  $\bar{C}$  is the average dislocation contrast factor ( $\bar{C} = 0.3$  for reflection 200),  $b$  is the magnitude of the Burgers-vector ( $b = 0.256$  nm),  $R_e$  is the outer cut-off radius of dislocations ( $R_e = 12$  nm for both the initial and the heat-treated foams as obtained by CMWP fitting), and  $L$  is the Fourier-length ( $L = 6$  nm was selected as the mean of the shortest ( $b$ ) and longest ( $R_e$ ) reasonable distances around dislocations). The average elastic strain calculated from this formula is 0.2–0.3% for both the initial and the heat-treated foams in accordance with similar measured dislocation densities and outer cut-off radii. It seems that the heat treatment did not cause significant change in the lattice strains even if a microstructure coarsening occurred.

In spite of the unchanged hardness, the surface indentation study (Figure 6) indicates an increase in the fracture toughness of the foam after annealing. Indeed, while cracks in the initial foam (Figure 6a) are seen to have formed due to caving under the punch during indentation, the heat-treated material (Figure 6b) remains free of visible cracks. The fracture toughness of a material characterizes the resistance against crack propagation; therefore, the fracture toughness surely increased due to the heat treatment even if this observation was made only qualitatively. It is noted that indentation can be used for the quantitative determination of fracture toughness for bulk materials. In this case, the toughness can be obtained from the hardness, the elastic modulus, and the length of the cracks developed in the vicinity of the indentation pattern [32]. The fracture toughness formulas proposed in the literature were elaborated for bulk materials; for their application, the shape of the cracks under the studied surface must be known. Thus, the quantitative determination of the fracture toughness from the crack length observed by optical microscopy is not possible in the present case.

The increase in the fracture toughness was most probably caused by a significant strengthening of the junctions between the ligaments. Indeed, previous studies have also suggested that coarsening of the microstructure (i.e., increase in ligament contiguity) in metallic foams might lead to decreased brittleness [33]. In particular, this effect has been observed in Cu nanofoams processed by dealloying from sintered material, where an increase in the sintering temperature led to simultaneous coarsening of the ligaments and increase in the degree of ligament continuity, thus improving the fracture toughness of the foam [19]. Despite the arguable negative effect (e.g., pinch-off [20]) of annealing on nanoporous metal, the benefit of annealing on the mechanical properties of metallic foams was also observed in some nanoporous metals such as gold, where the reduction of crack density and the increase of ligament size caused by coarsening contributed to the increase of the global strength [34]. It is worth noting that the foam ligaments may coarsen without changing the overall porosity, i.e., both the ligament and pore sizes may increase proportionally [35]. In this case, there is no densification-induced hardening effect, i.e., only the strengthening of the ligament junction and the healing of cracks are operative. Note that the annealing-induced toughening mechanisms that are operative in this study are also shown schematically in Figure 7.



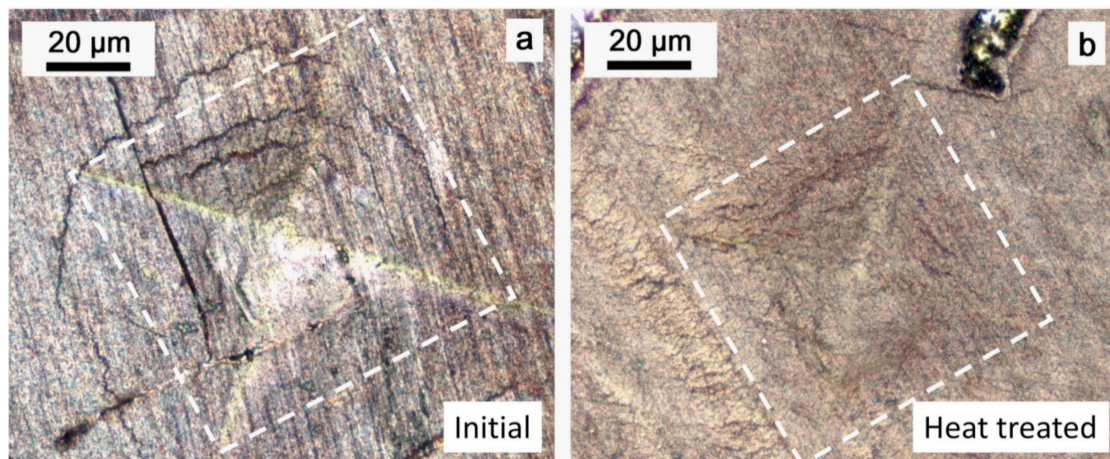


**Figure 6.** Surface patterns under the indenter after hardness measurement of the initial (a) and the heat treated (b) foams. The dashed white square indicates the surface area under the loaded indenter.

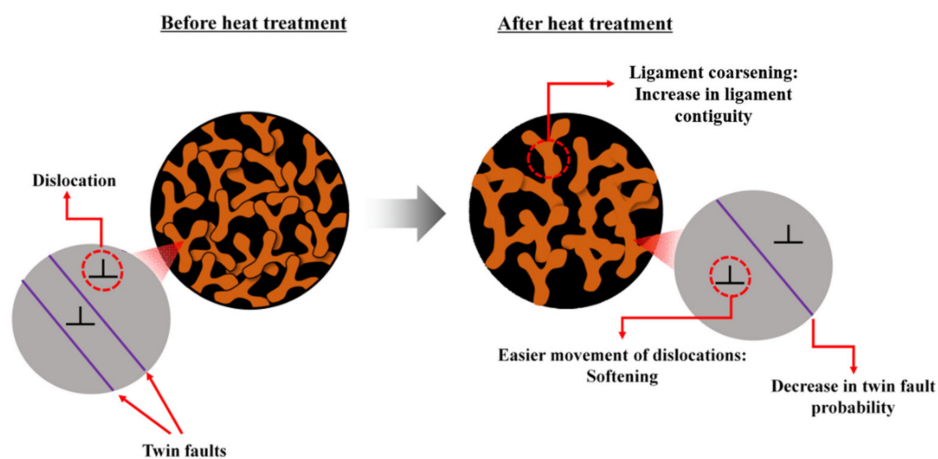


**Figure 7.** Schematic of the annealing-induced toughening mechanisms observed in this study, including ligament contiguity increase via ligament coarsening and softening via decrease of the twin fault probability.

#### 4. Conclusions

In summary, the present study demonstrated that heat treatment at a moderate temperature of 400 °C for 6 h resulted in the improvement of the resistance against crack propagation for a Cu nanofoam that was processed via the dealloying technique. Since the ligament size was only slightly changed and the oxide phase (anode active material) remained unchanged, it is expected that the electrochemical performance of this material in LIB applications should not be considerably altered. However, an additional set of systematic experiments are necessary to fully confirm this assumption. In addition, an optimization of the heat treatment condition (i.e., the temperature, time, and atmosphere of annealing) is required for obtaining the best combination of mechanical and electrochemical properties for the Cu nanofoam anode. This study also demonstrated that despite the arguable negative effect (e.g., pinch-off) of annealing on nanoporous metal, the benefits of annealing on the mechanical properties of our Cu nanofoam were clearly observed in the reduction of crack density, the increase of ligament size caused by coarsening, and the increase of contiguity, all contributing to the increase of the global strength.

**Author Contributions:** Conceptualization, H.C. and J.G.; methodology, G.H., H.C., P.J., and C.K.; validation, H.C.; formal analysis, P.J., C.K., P.T.H., G.H., and J.G.; investigation, P.J., C.K., and P.T.H.; resources, H.C. and J.G.; data curation, P.J., C.K., and P.T.H.; writing—original draft preparation, H.C. and J.G.; writing—review

and editing, G.H., P.J., P.T.H., and C.K.; visualization, G.H., P.J., and J.G.; supervision, H.C. and J.G.; funding acquisition, H.C. and J.G. All authors have read and agreed to the published version of the manuscript.

**Funding:** This research was supported by the Hungarian-Korean bilateral Research program (TÉT) No. 2018–2.1.17-TÉT-KR–2018–00003. This work was financed partly by the Ministry of Human Capacities of Hungary within the ELTE University Excellence program (1783–3/2018/FEKUTSRAT). Heeman Choe also acknowledges support from the International Research & Development Program of the National Research Foundation of Korea (2018K1A3A1A39086825). Péter Jenei acknowledges the financial support of ÚNKP–19–4 New National Excellence Program of the Ministry for Innovation and Technology. This paper was supported by the János Bolyai Research Scholarship of the Hungarian Academy of Sciences (Péter Jenei and Csilla Kádár).

**Conflicts of Interest:** The authors declare no conflict of interest.

## References

1. Goodenough, J.B.; Gao, H. A perspective on the Li-ion battery. *Sci. China Chem.* **2019**, *62*, 1555–1556. [[CrossRef](#)]
2. Poizot, P.; Laruelle, S.; Grugeon, S.; Dupont, L.; Tarascon, J.M. Nano-sized transition-metal oxides as negative-electrode materials for lithium-ion batteries. *Nature* **2000**, *407*, 496. [[CrossRef](#)] [[PubMed](#)]
3. Etacheri, V.; Marom, R.; Elazari, R.; Salitra, G.; Aurbach, D. Challenges in the development of advanced Li-ion batteries: A review. *Energy Environ. Sci.* **2011**, *4*, 3243. [[CrossRef](#)]
4. Sawai, K.; Iwakoshi, Y.; Ohzuku, T. Carbon materials for lithium-ion (shuttlecock) cells. *Solid State Ion.* **1994**, *69*, 273–283. [[CrossRef](#)]
5. Ji, L.; Lin, Z.; Alcoutlabi, M.; Zhang, X. Recent developments in nanostructured anode materials for rechargeable lithium-ion batteries. *Energy Environ. Sci.* **2011**, *4*, 2682–2699. [[CrossRef](#)]
6. Jiang, J.; Li, Y.; Liu, J.; Huang, X.; Yuan, C.; Lou, X.W. Recent Advances in Metal Oxide-based Electrode Architecture Design for Electrochemical Energy Storage. *Adv. Mater.* **2012**, *24*, 5166. [[CrossRef](#)]
7. Han, G.; Um, J.H.; Park, H.; Hong, K.; Yoon, W.S.; Choe, H. Hierarchically structured nanoporous copper for use as lithium-ion battery anode. *Scripta Mater.* **2019**, *163*, 9–13. [[CrossRef](#)]
8. Jo, H.; Kim, M.J.; Choi, H.; Sung, Y.-E.; Choe, H.; Dunand, D.C. Morphological study of directionally freeze-cast nickel foams. *Metall. Mater. Trans. E* **2016**, *3*, 46–54. [[CrossRef](#)]
9. Wang, Z.; Su, F.; Madhavi, S.; Lou, X.H. CuO Nanostructures supported on Cu substrate as integrated electrodes for highly reversible lithium storage. *Nanoscale* **2011**, *3*, 1618–1623. [[CrossRef](#)]
10. Zou, L.; Gan, L.; Kang, F.; Wang, M.; Shen, W.; Huang, Z. Sn/C non-woven film prepared by electrospinning as anode materials for lithium ion batteries. *J. Power Sources* **2010**, *195*, 1216–1220. [[CrossRef](#)]
11. Sun, L.; Chien, C.L.; Searson, P.C. Fabrication of nanoporous nickel by electrochemical dealloying. *Chem. Mater.* **2004**, *16*, 3125. [[CrossRef](#)]
12. Park, H.; Um, J.H.; Choi, H.; Yoon, W.S.; Sung, Y.E.; Choe, H. Hierarchical micro-lamella-structured 3D porous copper current collector coated with tin for advanced lithium-ion batteries. *Appl. Surf. Sci.* **2017**, *399*, 132–138. [[CrossRef](#)]
13. Lee, S.; Tam, J.; Li, W.; Yu, B.; Cho, H.J.; Samei, J.; Wilkinson, D.S.; Choe, H.; Erb, U. Multi-scale morphological characterization of Ni foams with directional pores. *Mater. Charact.* **2019**, *158*, 109939. [[CrossRef](#)]
14. Ribárik, G.; Gubicza, J.; Ungár, T. Correlation between strength and microstructure of ball-milled Al–Mg alloys determined by X-ray diffraction. *Mater. Sci. Eng. A* **2004**, *387–389*, 343–347.
15. Gubicza, J. *X-Ray Line Profile Analysis in Materials Science*; IGI-Global: Hershey, PA, USA, 2014.
16. Liu, W.; Zhang, S.; Li, N.; Zheng, J.; An, S.; Li, G. Influence of Dealloying Solution on the Microstructure of Monolithic Nanoporous Copper through Chemical Dealloying of Al 30 at.% Cu Alloy. *Int. J. Electrochem. Sci.* **2012**, *7*, 7993–8006.
17. Viswanathan, V.; Laha, T.; Balani, K.; Agarwal, A.; Seal, S. Challenges and advances in nanocomposite processing techniques. *Mater. Sci. Eng. R* **2006**, *54*, 121–285. [[CrossRef](#)]
18. Fan, Z.; Miodownik, A.P.; Tsakirooulos, P. Microstructural characterisation of two phase materials. *J. Mater. Sci. Technol.* **2013**, *7*, 1094–1100. [[CrossRef](#)]
19. Jo, H.; Cho, Y.H.; Choi, M.; Cho, J.; Um, J.H.; Yung-Eun Sung, Y.E.; Choe, H. Novel method of powder-based processing of copper nanofoams for their potential use in energy applications. *Mater. Chem. Phys.* **2014**, *145*, 6–11. [[CrossRef](#)]

20. Li, T.; Ngô, B.N.D.; Markmann, J.; Weissmuller, J. Topology evolution during coarsening of nanoscale metal network structures. *Phys. Rev. Mater.* **2019**, *3*, 076001. [[CrossRef](#)]
21. Liu, L.; Ye, X.; Jin, H. Interpreting anomalous low-strength and low-stiffness of nanoporous gold: Quantification of network connectivity. *Acta Mater.* **2016**, *18*, 77–87. [[CrossRef](#)]
22. Sun, Y.; Balk, J. A multi-step dealloying method to produce nanoporous gold with no volume change and minimal cracking. *Scr. Mater.* **2008**, *58*, 727–730. [[CrossRef](#)]
23. Geslin, P.; Buchet, M.; Wada, T.; Kato, H. Phase-field investigation of the coarsening of porous structures by surface diffusion. *Phys. Rev. Mater.* **2019**, *3*, 083401. [[CrossRef](#)]
24. Herring, C. Effect of Change of Scale on Sintering Phenomena. *J. Appl. Phys.* **1949**, *16*, 301–303. [[CrossRef](#)]
25. Um, T.; Wilke, S.K.; Choe, H.; Dunand, D.C. Effects of pore morphology on the cyclical oxidatio/-reduction of iron foams created via camphene-based freeze casting. *J. Alloys. Compd.* **2020**, *845*, 156278. [[CrossRef](#)]
26. Nam, K.; Park, H.; Choe, H. Continuity as a governing parameter to predict the strength of porous materials. *Mater. Lett.* **2018**, *214*, 99–102. [[CrossRef](#)]
27. Kolonits, T.; Czigány, Z.; Péter, L.; Bakonyi, I.; Gubicza, J. Influence of Bath Additives on the Thermal Stability of the Nanostructure and Hardness of Ni Films Processed by Electrodeposition. *Coatings* **2019**, *9*, 644. [[CrossRef](#)]
28. Kapoor, G.; Péter, L.; Fekete, É.; Lábár, J.L.; Gubicza, J. The influence of Mo addition on the microstructure and its thermal stability for electrodeposited Ni films. *Mater. Charact.* **2018**, *145*, 563–572. [[CrossRef](#)]
29. Nunes, A.C.; Lin, D. Effects of surface relaxation on powder diffraction patterns of very fine particles. *J. Appl. Cryst.* **1995**, *28*, 274–278. [[CrossRef](#)]
30. Leoni, M.; Scardi, P. Grain surface relaxation effects in powder diffraction. In *Diffraction Analysis of the Microstructure of Materials*; Scardi, P., Mittemeijer, E.J., Eds.; Springer Science & Business Media: Berlin, Germany, 2004.
31. Zhang, C.L.; Godfrey, A.; Zhang, Y.; Wu, G.L.; Xu, R.; Liu, W.; Juul Jensen, D. Dislocation density in fine grain-size spark-plasma sintered aluminum measured using high brightness synchrotron radiation. *Mater. Lett.* **2020**, *269*, 127653. [[CrossRef](#)]
32. Gubicza, J. Characterization of glasses and ceramics by continuous indentation tests. *Key Eng. Mater.* **1995**, *103*, 217–220. [[CrossRef](#)]
33. Biener, J.; Hodge, A.M.; Hayes, J.R.; Volkert, C.A.; Zepeda-Ruiz, L.A.; Hamza, A.V.; Abraham, F.F. Size Effects on the Mechanical Behavior of Nanoporous Au. *Nano Lett.* **2006**, *6*, 2379–2382. [[CrossRef](#)] [[PubMed](#)]
34. Cox, M.E.; Dunand, D.C. Bulk gold with hierarchical macro-, micro- and nano-porosity. *Mater. Sci. Eng. A* **2011**, *528*, 2401–2406. [[CrossRef](#)]
35. Chen-Wiegart, Y.K.; Wang, S.; Chu, Y.S.; Liu, W.; McNulty, I.; Voorhees, P.W.; Dunand, D.C. Structural evolution of nanoporous gold during thermal coarsening. *Acta Mater.* **2012**, *60*, 4972–4981. [[CrossRef](#)]

